High potential for splay faulting in the Molucca Sea, Indonesia: November 2019 M_w7.2 earthquake and tsunami

Mohammad Heidarzadeh[1,*], Takeo Ishibe[2], Tomoya Harada[3], Danny Hilman Natawidjaja[4], Ignatius Ryan Pranantyo[1], Bayu Triyogo Widyantoro[5]

[1]Department of Civil & Environmental Engineering, Brunel University London, Uxbridge UB8 3PH, UK
[2]Association for the Development of Earthquake Prediction, Tokyo 101-0064, Japan
[3]Horihune 1-12-11, Kita-ku, Tokyo 114-0004, Japan
[4]RC Geotechnology, Indonesian Institute of Sciences (LIPI), Bandung 40135, Indonesia
[5]The Indonesian Geospatial Information Agency, Cibinong, Indonesia

Accepted for publication in: ***"Seismological Research Letters"***
Acceptance date: April 2021
doi: https://doi.org/10.1785/0220200442

* Correspondence to:

Mohammad Heidarzadeh, PhD
Associate Professor
Department of Civil & Environmental Engineering,
Brunel University London,
Uxbridge, UB8 3PH
UK.
Email: mohammad.heidarzadeh@brunel.ac.uk
Website: https://www.brunel.ac.uk/people/mohammad-heidarzadeh
ORCID: https://orcid.org/0000-0002-1112-1276

Abstract:

Tsunami potential from high dip-angle splay faults is an understudied topic, although such splay faults can significantly amplify coastal tsunami heights as compared to ordinary thrust faults. Here, we identify a hot spot for tsunamis from splay faulting in the Molucca Sea arc-arc collision zone in eastern Indonesia which accommodates one of the world's most complicated tectonic settings. The November 2019 M_w7.2 earthquake and tsunami are studied through teleseismic inversions assuming rupture velocities in the range 1.5 – 4.0 km/s followed by tsunami simulations. The Normalized Root-Mean Square Error index was applied which revealed that the best model has a rupture velocity of 2.0 km/s from the steeply-dipping plane. The recent high dip-angle reverse earthquakes of 2019 M_w7.2 and 2014 M_w7.1 combined with numerous similar seismic events may indicate that this region is prone to splay faulting. This study highlights the need for understanding tsunamis from splay faulting in other world's subduction zones.

Keywords:

Tsunami; Earthquake; Eastern Indonesia; Numerical Simulations; Seismicity; Divergent Double Subduction Zone; Teleseismic Inversion.

1. Introduction

The unusually-large tsunami hazard from splay faulting was first identified during the 1964 Alaska M_w 9.2 earthquake and tsunami where 12 m of crustal deformation was reported locally from the Fatton Bay splay fault while the maximum deformation on neighboring plate-boundary segments was 6 m (Plafker, 1972). Splay faulting was also reported for other major earthquakes such as: 1944 Tonankai (Baba et al., 2006), 1946 Nankai (Cummins & Kaneda, 2000) and 2004 Sumatra-Andaman (Sibuet et al., 2007). As splay faults are characterized by steep dip angles, they effectively produce high tsunamis, especially in the near-field. Through numerical modeling, Heidarzadeh et al. (2009) showed that tsunami heights can be significantly amplified locally by considering splay faulting during subduction-zone thrust earthquakes. Rupture on splay faults and its interaction with plate boundary rupture is a complex process (Park et al., 2002; Sykes & Menke, 2006; Baba et al., 2006). Among various unknowns on splay fault ruptures, one question is that whether they can rupture independent of plate-boundary earthquakes or not (Sykes and Menke, 2006).

The Molucca Sea (eastern Indonesia, Figure 1) appears to be a hot spot for splay faulting; thus studying seismic and tsunami activities in this region may help to improve our understanding of tsunamigenesis of splay faults. On 14 November 2019, a large earthquake with a moment magnitude (M_w) of 7.2 occurred in this region (Figure 1a). Based on the United States Geological Survey (USGS), the epicenter of the earthquake was at 1.621^{o}N and 126.416^{o}E occurring at 16:17:40 UTC with a depth of 33.0 km (Figure 1). The focal mechanism solution by the USGS indicates a reverse-type earthquake mechanism with the strike/dip and rake angles of 224^o/50^o and 102^o, respectively, for the first nodal plane (NP-1) and corresponding values of 25^o/42^o and 76^o for the second plane (NP-2). USGS determined M_w of 7.1 for this event; however, our analysis resulted in M_w 7.2, which is used hereafter. The Global Centroid Moment Tensor project (GCMT, Ekström et al., 2012) calculated an M_w of 7.1 for this earthquake with focal mechanism solutions of 15^o/39^o (strike/dip) and 67^o (rake) for NP-1 and respective values of 223^o/55^o and 107^o for NP-2. The focal depth is reported 31.2 km by GCMT. According to media reports, the earthquake caused some damage to buildings and left a few injuries. A small tsunami was generated following this earthquake whose coastal height was a few tens of centimeters (Figures 2, 3).

Eastern Indonesia and, in particular, the Molucca Sea region is characterized by complicated tectonic settings where a number of curved subduction zones (SZ) and major faults intersect each other; namely, the north Sulawesi SZ, the two parallel SZs of Sangihe and Halmahera, and the Philippine SZ (Figure 1) (Hall, 2002; Hall & Smyth, 2008). The two parallel SZs of Sangihe and Halmahera form an underlying divergent double SZ with a blanketing active arc-arc collision (Figure 1b). It is shown that the crust between these two SZs and above the Molucca Sea plate is characterized by numerous steep reverse faults (Hall & Smyth, 2008; Gunawan et al., 2016). These features are called splay faults by Gunawan et al. (2016) and Gusman et al. (2017). Imbricate splay faults are steep reverse faults that emanate from a basal low-angle thrust upwards to the seafloor (Plafker, 1972) and pose major tsunami hazards (Heidarzadeh, 2011). As a result of such a complicated tectonic setting, the area hosts intensive earthquake and tsunami activities (Figure 4; Table 1). In their catalogue of tsunamis in Indonesia, Latief et al. (2000) marked the Molucca Sea region as the second most-active tsunamigenic zone hosting 31% of all tsunamis and responsible for the deaths of 7576 people till 1999 AD. As examples, the 1998 and 1965 tsunamis in this region killed 34 and 71 people, respectively (Latief et al., 2000). On 15 November 2014, a similar reverse-type mechanism earthquake (M_w 7.1) occurred close to the 2019 epicenter (Figure 1) which generated a small tsunami (Gusman et al., 2017).

Here, we briefly investigate the regional seismotectonics and past seismicity, analyze aftershocks of the November 2019 earthquake and analyze the actual sea level records of the November 2019 tsunami. We develop a source model for the earthquake based on teleseismic inversion combined with forward tsunami modeling and discuss the potential for splay faulting in the Molucca Sea region.

2. Data and Methods

The data consists of tide gauge records, teleseismic waves and earthquake aftershocks. Tsunami tide gauge data are provided by the Agency for Geo-spatial Information, Indonesia (BIG), with sampling intervals of 1 min. A total number of 16 tide gauge data were analyzed in this study (Figure 2); however, tsunami signals were clear in eight stations (Figure 3). Tide gauge data underwent quality control for spikes in data. Tsunami waveforms were detected after removing the tidal signals by applying the tidal prediction package TIDALFIT (Grinsted, 2008). The maximum zero-to-crest tsunami amplitudes are: 13.6 cm (Bitung), 5.3 cm (Ternate), 7.0 cm (Jailolo), 4.0 cm (Tidore), 7.1 cm (Manado), 8.9 cm (Tahuna), ~5 cm (Melonguane), and 4.8 cm (Taliabu). For aftershock data, we benefited from the public earthquake catalogue database of the USGS. Our teleseismic data came from the Incorporated Research Institutions for Seismology (IRIS). We used 69 teleseismic records comprising of 63 P and 6 SH waves (see Figure 1 for locations, and Figures S1 and S2 for waveforms). A bandpass filter of 0.004−1.0 Hz was applied to all teleseismic data. The velocity structures provided by CRUST 1.0 (Laske et al., 2013) and ak135 (Kennett et al., 1995) were applied for teleseismic inversion. Our teleseismic inversion was conducted for 60 s of the records (Figures S1-2).

Our methodology is a combination of teleseismic source inversion, aftershock analysis and forward tsunami modeling. For teleseismic body wave inversion, we followed the 2003-updated version of the numerical package by Kikuchi & Kanamori (1991). The finite-fault slip models were calculated for both Nodal Planes (NP): the lower-angle plane with a dip angle of 39^o (NP-1) and the steeper one with a dip angle of 55^o (NP-2). The sub-faults dimensions were 5 km (strike-wise) × 5 km (dip-wise). The total number of sub-fault used for inversion varied from 72 (for V_r =1.5 km/s) to 189 (for V_r =4.0 km/s). For each sub-fault, we considered maximum rupture duration of 5 s which is a combination of four rise-time triangles: each triangle was given duration of 2 s and was overlapped by 1 s with the adjacent triangle. As estimation of rupture velocity (V_r) of earthquakes is associated with uncertainties, we varied V_r in the range of 1.5−4.0 km/s with 0.5 km/s intervals. This gives six finite-fault slip models for each NP and 12 models for both NPs. For each teleseismic inversion, quality of fit between synthetic teleseismic waveforms and real observations was evaluated through the Normalized Root-Mean Square Error (NRMSE) index (Heidarzadeh et al., 2016a, 2020):

$$NRMSE_k = \frac{\sqrt{\sum_{i=1}^{N}(obs_i - sim_i)^2}}{\sqrt{\sum_{i=1}^{N}(obs_i - \overline{obs})^2}} \quad (1)$$

where $NRMSE_k$ represents the Normalized Root Mean Square Error for station number k, and the counter $i = 1,2, \ldots, N$, shows the sampled waveforms where N is the total number of the records at a particular station. The two variables obs_i and sim_i represent observed and simulated values, respectively. Also, the average value of observations is represented by $\overline{obs}$.

It has been reported that teleseismic inversion results are sensitive to the choice of V_r and thus it is recommended to further constrain them by other geophysical data such as tsunami and geodetic data (e.g. Lay et al. 2014; Gusman et al. 2015; Satake & Heidarzadeh, 2017; Satake et al., 2013; Heidarzadeh et al. 2016b). This has been done in this study by employing earthquake aftershock data and tsunami sea level observations. For aftershock analysis, we plotted distribution of focal depths in the normal direction to the fault strike and evaluated the depth trend with regard to dip angle. By performing aftershock analysis for the two NPs, it may reveal which NP is more consistent with aftershock focal depth patterns.

Forward tsunami simulations were conducted by the Nonlinear Shallow Water package of COMCOT (Cornell Multi-grid Coupled Tsunami Model) (Liu et al., 1998; Wang & Liu, 2006). Our tsunami model is non-dispersive because long tectonic tsunami sources do not usually show dispersive characters (Heidarzadeh et al., 2014). Bathymetry data is provided by the 2019 edition of the General Bathymetric Chart of the Oceans (GEBCO) which comes with 15 arc-sec spatial resolution (Weatherall et al., 2015). We used a single uniformly-spaced bathymetry grid with spatial resolution of 15 arc-sec. The time step for finite difference calculations was 0.5 s. The dislocation model of Okada (1985) was applied for calculation of initial coseismic crustal deformation. Similar to teleseismic inversions, the quality of match between simulated tsunami waveforms and tide gauge observations were examined through the NRMSE index.

3. Seismotectonics, past seismicity and aftershock focal depth analysis

The Molucca Sea region, between the Sangihe and the Halmahera Island arcs, is located on an underlying complex tectonic structure that has been subjected to a fast plate convergence rate, enabling the generation of numerous large earthquakes and tsunamis (Figure 4a). The submarine top crust (Figure 1b) is an arc-arc collision resulted from the shortening due to the underlying double-verging subductions eastward and westward of the Molucca Sea Plate (Silver & Moore, 1978; Moore et al., 1981; Hall & Wilson, 2000). The collision process has resulted in the formation of imbricated reverse-fault zones striking generally north-south and dipping towards both west and east (Figure 1b). Based on geological studies, visual inspections of bathymetry and seismic reflection profiles, it has been postulated that the collision zone is presently predominated by the Sangihe fore-arc overriding the Halmahera fore-arc eastward; therefore, resulting in the accretionary complex of thrust dipping westward.

The collision and shortening processes is ongoing with a convergence rate of 76 – 80 mm/year (Socquet et al., 2006). Such a fast convergence is capable of producing an M7 earthquake, similar to the 2019 (M_w7.2) event, every 10 – 20 years assuming an average coseismic slip of 1.2 ± 0.4 m, based on the empirical relationship from Wells & Coppersmith (1994). This preliminary calculation is well correlated with the high occurrence of large earthquakes in this region. Several large earthquakes have occurred in the Molucca Sea in the past (Table 1): 2019 (M_w7.2), 2014 (M_w7.1), 2000 (M7.6), 1986 (M7.5), 1979 (M6.8), 1936 (M7.8), 1932 (M7.7) and 1913 (M7.8). Therefore, on average, there is one M7 event every one to two decades. The penultimate large earthquake (M_w7.1) occurred on November 15, 2014, and its aftershocks were studied by Shiddiqi et al. (2015) who found that the mainshock mechanism was high dip-angle reverse fault with strike/dip of 192°/55°.

The focal mechanism solutions for earthquakes since 1976 from the GCMT project indicate that the reverse-type focal mechanisms striking roughly NNE-SSW directions are dominant in the Molucca Sea region (Figures 1 and 4). The 2019 Molucca Sea earthquake had a similar focal mechanism solution as observed before. For this 2019 event, cross sections of the one-month aftershocks perpendicular to each nodal plane (Figure 4b) indicate that it is not straightforward to distinguish which nodal plane is the actual fault due to the limited accuracy in hypocentral depth. The spatial extent of the one-month aftershocks can be used for constraining the dimension of the fault rupture.

4. Earthquake source model and hazard implications

We obtained 12 source models for two nodal planes NP-1 and NP-2 by varying V_r in the range of 1.5−4.0 km/s (Figures 5, S3 and S4). The slip values for various models are up to 6 m: the larger the V_r is, the smaller the maximum slip value of a source model is (Figure 5). The teleseismic NRMSE ranges from 0.6467 to 0.6615, showing small variations (Figure 5j). The high dip-angle nodal plane (NP-2) yields smaller NRMSEs than the lower-angle fault plane (NP-1), indicating that NP-2 is possibly the actual fault plane of the earthquake. The minimum teleseismic NRMSE belongs to the model with V_r=3.0 km/s for NP-2 (Figure 5j). Although the plot of teleseismic NRMSE of NP-2 has a minimum point and guides the best model, it may not be considered as reliable enough because the domain of NRMSE variations is small (i.e. ~0.01). Therefore, it was necessary to further validate the choice of the best model using another type of data; i.e. tsunami observations.

Numerical modeling of tsunami was performed for all 12 models (Figures 6, S5 and S6) and the NRMSE between observations and simulations were calculated (Figure 6d). Similar to teleseismic inversions, the high dip-angle nodal plane (NP-2) gives smaller tsunami NRMSEs than the lower-angle fault plane (NP-1). The NRMSEs for the NP-2 are clearly separated from those of NP-1 with an average gap of ~0.2 (Figure 6d). Therefore, we concluded that the high dip-angle nodal plane (NP-2) is the actual fault plane. According to tsunami simulations, the best model is the one with V_r=2.0 km/s for the high dip-angle nodal plane (NP-2) (Figure 6d), while it was V_r=3.0 km/s based on teleseismic inversion (Figure 5j). The slower velocity from tsunami data implies that the tsunami source area and the coseismic displacement field are smaller than that predicted by seismic data (Figure 5).

We note that the match between simulated and modeled tsunami waveforms is not perfect (Figure 6a) for several reasons. The primary reason can be attributed to the small size of the event and the fact that observed tsunami waveforms are approximately in the range of ±10 cm; for some stations the amplitudes are close to the noise level (Figures 2-3). The second reason could be the complex bathymetry of the region and the presence of several islands whose precise bathymetry is not available currently. Nevertheless, this is not a barrier for this study because here we aimed at a comparative study of the performance of different models rather than producing a perfect match between observations and simulations.

To choose the final model, we used a weighted NRMSE by considering 33.3% and 66.7% for the weights of the teleseismic and tsunami NRMSEs, respectively (Figure 7a). We note that the choice of weights for the teleseismic and tsunami misfits has been a challenging task in earthquake/tsunami source studies. While some authors used equal weights (e.g. Yokota et al., 2011), many others gave larger weights to tsunami data (e.g. Satake 1987; Lay et al., 2014; Gusman et al., 2015; Heidarzadeh et al., 2016b). As discussed by Satake (1987), tsunami data give more reliable estimates of spatial distribution of earthquake sources and thus must be given larger weights. This observation by Satake (1987) has been validated by several later studies (e.g. Lay et al., 2014; Gusman et al., 2015; Heidarzadeh et al., 2016a, b). Therefore, we give the higher weight of 66.7% to tsunami data in this study (Figure 7a).

Such a weighted NRMSE led to V_r=2.0 km/s of the high dip-angle nodal plane (NP-2) as the final model (Figure 7a). The spatial extent of one-month aftershocks is consistent with the fault models with slow V_r (e.g., 1.5 − 2.0 km/s). The final slip model is shown in Figure 6b, and its coseismic crustal deformation is given in Figure 6c. The maximum slip is 2.9 m and the average slip on the non-zero sub-faults is 0.64 m (Figure 6b). The seismic moment associated with this final slip model is 7.64×10^{19} Nm, equivalent to M_w7.2. Distribution of maximum tsunami amplitude (Figure 7d) reveals that they are concentrated along the normal direction to the fault strike as expected from tsunami's directivity (e.g. Ben-Menahem and Rosenman, 1972).

Analysis of the 15 November 2014 Molucca Sea M_w 7.1 earthquake revealed that the actual fault plane was a steeply west-dipping fault with a dip angle of 65^o (Figure 7c) (Gunawan et al., 2016). The November 2014 and November 2019 earthquakes, both having high dip-angle fault planes, are two independent earthquakes in the Molucca Sea region that share the characteristic feature of rupturing along steep fault planes. They may indicate that the Molucca Sea zone is prone to these types of high dip-angle reverse faulting due to crustal shortening (Figure 1b). The region frequently produces reverse-fault earthquakes (Figure 4; Table 1). Although the source models for other thrust earthquakes in the area are unavailable, they likely follow the same behavior of rupturing along high-angle reverse faults; e.g. the 2007 M_w7.5 event (Figure 7c).

5. Discussion

The generation of high dip-angle reverse-fault earthquakes is unfavorable with the Anderson's (1905) theory of faulting where the principal and least stresses σ_1 and σ_3 are horizontal and vertical, respectively; however, these types of faulting commonly occur worldwide. The high dip-angle reverse faulting can occur in different circumstances, such as: (i) compressional inversion of inherited normal faults (e.g., Sibson & Xie, 1998; Wu et al., 2014); (ii) steepening of the original low dip-angle thrust as they became frictionally locked and rotated during shortening such as those commonly occurring in accretionary wedges ; (iii) steepening fault dips by block rotations; and (iv) formation of steep-angle splay faults above the main low dip-angle thrust fault or basal thrust as reported by Gunawan et. al (2016). For the Molucca Sea region, point (i) is not the case because the area is of a compressional tectonic regime. Point (ii) is a common feature of active accretionary wedges in subduction zones, and thus is not the case here. For the Molucca overriding crustal shortening due to the sinking active double subduction zone, point (iv) seems to be the most preferred model; however, point (iii) (block rotations) might also be relevant. The steep reverse faulting might occur on (meta) sedimentary rocks on the overriding (continental) Sangihe crust. The relatively slow rupture, as modelled in this study, might be facilitated by high pore pressures associated with fluid flows from the overlying ocean. Future studies, such as obtaining multi-channel seismic reflection data are necessary to shed lights on this issue and to provide more information on actual fault geometries and rock types.

Returning to the original question on whether splay faulting can generate a large earthquake and tsunami independent of plate-boundary rupture or not, analysis of seismicity in the Molucca Sea region shows that large earthquakes due to splay faulting can occur independently here; this is probably because of thick seismogenic zone (up to ~60 km; Figure 1b) which contributes maximum fault width and fault rupture area (e.g. Wells & Coppersmith, 1994). From the tsunami hazard point of view, splay faulting must be considered for earthquake and tsunami scenarios in the Molucca Sea region. Any tsunami hazard analyses without considering splay faulting may significantly underestimate the tsunami hazards. Globally, the Molucca Sea's seismic behavior is a reminder of high tsunami potential from splay faulting and the need to properly understand such potential in other world's tsunamigenic zones.

6. Conclusions

We analyzed the 14 November 2019 M_w7.2 earthquake and associated tsunami in the Molucca Sea arc-arc collision zone using teleseismic and tsunami data. Main findings are:

(i) The earthquake occurred in the active arc-arc collision zone where large earthquakes frequently have been occurring. The spatial extent of the one-month aftershocks is approximately consistent with the fault model with slow rupture velocity (V_r) of 1.5 –2.0 km/s, while it is not straightforward to distinguish which nodal plane is an actual source fault from only aftershock distributions.

(ii) By applying teleseismic inversions and through varying V_r in the range 1.5 – 4.0 km/s, we obtained 12 source models. The Normalized Root-Mean Square Error (NRMSE) index showed that the nodal plane 2 (NP-2) gives better fitting to the observed waveforms than NP-1; however, the teleseismic NRMSEs were incapable of reliably guiding the best model because the range of variations of NRMSE was small (i.e. ~0.01) for different V_r.

(iii) By performing tsunami simulations, tsunami NRMSEs were calculated which revealed that NP-2 is better than NP-1 with a clear average gap of ~0.2. Therefore, both teleseismic and tsunami NRMSEs favored NP-2 over NP-1 as the actual fault plane of the earthquake. To choose the best model among the six models of NP-2, we used different weights of 33.3% and 66.7% for the seismic and tsunami data, respectively, which guided the best model of V_r =2.0 km/s.

(iv) Given the fact that two earthquakes, November 2019 (M_w7.2) and November 2014 (M_w7.1), combined with numerous similar seismic events, ruptured on high dip-angle reverse faults in the Molucca Sea collision zone may indicate that this region is prone to splay faulting. Source modeling for other thrust/reverse earthquakes in this region, including the 2007 M_w7.5 event, may help to further confirm this observation.

(v) Splay faulting has the potential to significantly amplify tsunami heights and thus it is necessary to be considered while planning earthquake/tsunami hazard studies in the Molucca Sea region. Recurrence of splay faulting in the Molucca Sea is a reminder of high tsunami potential from this seismic phenomenon; it is essential to investigate such potential in other world’s tsunamigenic zones.

Data and Resources

All data used in this study (i.e. tsunami waveforms, teleseismic waveforms, aftershocks) were downloaded from publicly-available websites which are: https://www.iris.edu/hq/ (for teleseismic waveforms); http://tides.big.go.id (for tsunami waveforms) and https://earthquake.usgs.gov/earthquakes/search/ (for aftershock data). Readers can access the data through the aforesaid three public websites. Supplemental Material for this article includes six figures which are: Figure S1 (teleseismic waveforms for nodal plane 1); Figure S2 (teleseismic waveforms for nodal plane 2); Figure S3 (all slip models for nodal plane 1); Figure S4 (all slip models for nodal plane 2); Figure S5 (tsunami simulations for various slip models of nodal plane 1) and Figure S6 (tsunami simulations for various slip models of nodal plane 2).

Conflict of interest

The authors declare that they have no competing interests.

Acknowledgements

We used the GMT software of Wessel & Smith (1998) in this study. We are very grateful to the Editor-in-Chief, Prof Allison Bent, and two anonymous reviewers for their constructive review comments. This research is funded by the Royal Society (The United Kingdom), grant number CHL\R1\180173.

References

Anderson, E. M., (1905). The dynamics of faulting, *Trans. Edinburgh Geol. Soc.* **8**(3), 387-402.

Baba, T., Cummins, Ph., Hori, T., & Kaneda, Y. (2006). High precision slip distribution of the 1944 Tonankai earthquake inferred from tsunami waveforms: Possible slip on a splay fault, *Tectonophys.* **426**, 119–134.

Ben-Menahem, A. and Rosenman, M., (1972). Amplitude patterns of tsunami waves from submarine earthquakes, *J. Geophys. Res.* **77**(17), 3097-3128.

Cummins, Ph., & Kaneda, Y. (2000). Possible splay fault slip during the 1946 Nankai earthquake, *Geophys. Res. Lett.* **27**, 2725–2728.

Ekström, G., Nettles, M., & Dziewonski, A. M. (2012). The global CMT project 2004-2010: Centroid-moment tensors for 13,017 earthquakes, *Phys. Earth Planet. Int.* **200-201**, 1-9. doi:10.1016/j.pepi.2012.04.002.

Grinsted, A. (2008). Tidal Fitting Toolbox. Accessed11 January 2020. https://uk.mathworks.com/matlabcentral/fileexchange/19099-tidal-fitting-toolbox?focused=3854016&tab=function&s_tid=gn_loc_drop.

Gunawan, E., Kholil, M., & Meilano, I. (2016). Splay-fault rupture during the 2014 Mw7. 1 Molucca Sea, Indonesia, earthquake determined from GPS measurements, *Phys. Earth Planet. Int.* **259**, 29-33.

Gusman, A. R., Murotani, S., Satake, K., Heidarzadeh, M., Gunawan, E., Watada, S., & Schurr, B. (2015). Fault slip distribution of the 2014 Iquique, Chile, earthquake estimated from ocean-wide tsunami waveforms and GPS data, *Geophys. Res. Lett.* **42**, 1053-1060.

Gusman, A.R., Nugraha, A.D., & Shiddiqi, H.A. (2017). Hypocenter relocations and tsunami simulation for the 15 November 2014 Northern Molucca Sea earthquake in Indonesia, *J. Geofisika* **15**(3), 1-9.

Hall, R. a., & Wilson, M. E. J. (2000). Neogene sutures in eastern Indonesia, *J. Asian Earth Sci.* **18**, 781-808.

Hall, R. (2002). Cenozoic geological and plate tectonic evolution of SE Asia and the SW Pacific: computer-based reconstructions, model and animations, *J. Asian Earth Sci.* **20**(4), 353-431.

Hall, R., & Smyth, H.R. (2008). Cenozoic arc processes in Indonesia: Identification of the key influences on the stratigraphic record in active volcanic arcs. In: Formation and applications of the sedimentary record in arc collision zones, Draut et al. (Editors), **436**, p.27.

Heidarzadeh, M., Pirooz, M.D., Zaker, N.H., & Yalciner, A.C. (2009). Modeling the near-field effects of the worst possible tsunami in the Makran subduction zone. *Ocean Eng.* **36** (5), 368–376.

Heidarzadeh, M. (2011). Major tsunami risk from splay faulting. In: The Tsunami Threat – Research and Technology, Morner, N.A. (Editor), Chapter 5, 67-80. ISBN: 978-953-307-552-5, INTECH International publishing.

Heidarzadeh, M., Krastel, S., & Yalciner, A. C. (2014). The State-of-the-Art Numerical Tools for Modeling Landslide Tsunamis: A Short Review. In: *Submarine Mass Movements and Their Consequences*, Chapter 43, 483-495, ISBN: 978-3-319-00971-1, Springer International publishing.

Heidarzadeh, M., Murotani, S., Satake, K., Ishibe, T., & Gusman, A.R. (2016a). Source model of the 16 September 2015 Illapel, Chile Mw 8.4 earthquake based on teleseismic and tsunami data, *Geophys. Res. Lett.* **43** (2), 643–650.

Heidarzadeh, M., Harada, T., Satake, K., Ishibe, T., & Gusman, A. (2016b). Comparative study of two tsunamigenic earthquakes in the Solomon Islands: 2015 Mw 7.0 normal-fault and 2013 Santa Cruz Mw 8.0 megathrust earthquakes, *Geophys. Res. Lett.* **43** (9), 4340–4349.

Heidarzadeh, M., Ishibe, T., Sandanbata, O., Muhari, A., Wijanarto, A.B. (2020). Numerical modeling of the subaerial landslide source of the 22 December 2018 Anak Krakatoa volcanic tsunami, Indonesia. *Ocean Eng.* **195**, https://doi.org/10.1016/j.oceaneng.2019.106733.

Kennett, B. L. N., Engdahl, E. R., & Buland, R. (1995). Constraints on seismic velocities in the Earth from travel times, *Geophys. J. Int.* **122**, 108–124.

Kikuchi, M., & H. Kanamori (1991), Inversion of complex body waves—III, *Bull. Seismol. Soc. Am.* **81**(6), 2335–2350.

Laske, G., Masters, G., Ma, Z., & Pasyanos, M. (2013). Update on CRUST1.0-A 1-degree Global Model of Earth's Crust, In: Geophysical Research Abstracts, **15**, Abstract EGU2013-2658.

Latief, H., Puspito, N.T., & Imamura, F. (2000). Tsunami catalog and zones in Indonesia, *J. Natural Disaster Sci.* **22**(1), 25-43.

Lay, T., Yue, H., Brodsky, E. E., & An, C. (2014). The 1 April 2014 Iquique, Chile, M w 8.1 earthquake rupture sequence, *Geophys. Res. Lett.* **41**, 3818–3825.

Liu, P. L.-F., Woo, S.-B., & Cho, Y.-S. (1998). Computer programs for tsunami propagation and inundation, Technical Report, Cornell University, Ithaca, N.Y.

Moore, G. F., Kadarisman, D., Evans, C. A., & Hawkins, J. W. (1981). Geology of the Talaud islands, Molucca sea collision zone, northeast Indonesia, *J. Structural Geol.* **3**(4), 467-475.

Okada, Y. (1985). Surface deformation due to shear and tensile faults in a half-space, *Bull. Seismol. Soc. Am.* **75**, 1135–1154.

Park, J.-O., Tsuru, T., Kodaira, S., Cummins, Ph., & Kaneda, Y. (2002). Splay fault branching along the Nankai subduction zone, *Science* **297**, 1157-1160.

Plafker, G. (1972). Alaskan earthquake of 1964 and Chilean earthquake of 1960: Implications for arc tectonics, *J. Geophys. Res.* **77**(5), 901-925.

Satake, K. (1987). Inversion of tsunami waveforms for the estimation of a fault heterogeneity: Method and numerical experiments, *J. Phys. Earth* **35**(3), 241–254.

Satake, K., Fujii, Y., Harada, T., & Namegaya, Y. (2013). Time and space distribution of coseismic slip of the 2011 Tohoku earthquake as inferred from tsunami waveform data, *Bull. Seismol. Soc. Am.* **103**(2B), 1473-1492.

Satake, K., & Heidarzadeh, M. (2017). A review of source models of the 2015 Illapel, Chile earthquake and insights from tsunami data, *Pure Appl. Geophys.* **174** (1), 1-9.

Shiddiqi, H. A., Widiyantoro, S., Nugraha, A. D., Ramdhan, M., Wiyono, S. H., & Wandono, W. (2015). Analysis of Mw 7.2 2014 Molucca Sea earthquake and its aftershocks, In: AIP Conference Proceedings **1730**, 020010 (2016); https://doi.org/10.1063/1.4947378.

Sibuet, J.C., Rangin, C., Le Pichon, X., Singh, S., Cattaneo, A., Graindorge, D., Klingelhoefer, F., Lin, J.Y., Malod, J., Maury, T. & Schneider, J.L., (2007). 26th December 2004 great Sumatra–Andaman earthquake: Co-seismic and post-seismic motions in northern Sumatra, *Earth Planet. Sci. Lett.* **263**(1-2), 88-103.

Sibson, R. H., & Xie, G. (1998). Dip range for intracontinental reverse fault ruptures: Truth not stranger than friction?, *Bull. Seismol. Soc. Am.* **88**(4), 1014-1022.

Silver, E. A., & Moore, J. C. (1978). The Molucca sea collision zone, Indonesia, *J. Geophys. Res.* **83**(B4), 1681-1691.

Socquet, A., Simons, W., Vigny, C., McCaffrey, R., Subarya, C., Sarsito, D., Ambrosius, B., & Spakman, W. (2006). Microblock rotations and fault coupling in SE Asia triple junction (Sulawesi, Indonesia) from GPS and earthquake slip vector data, *J. Geophys. Res.* **111**(B8). https://doi.org/10.1029/2005JB003963.

Sykes, L.R., & Menke, W. (2006). Repeat times of large earthquakes: implications for earthquake mechanics, *Bull. Seismol. Soc. Am.* **96**, 5, 1569– 1596.

Wang, X., & Liu, P. L.-F. (2006). An analysis of 2004 Sumatra earthquake fault plane mechanisms and Indian Ocean tsunami, *J. Hydraulic Res.* **44**, 147-154.

Weatherall, P., Marks, K.M., Jakobsson, M., Schmitt, T., Tani , S., Arndt, J.E., Rovere, M., Chaye, D. , Ferrini, V., & Wigley, R. (2015). A new digital bathymetric model of the world's oceans, *Earth Space Sci.* **2**, 331–345.

Wells, D. L., & Coppersmith, K. J., (1994). New empirical relationships among magnitude, rupture length, rupture width, rupture area, and surface displacement, *Bull. Seismol. Soc. Am.* **84**(4), 974-1002.

Wessel P., & Smith, W.H.F. (1998). New, improved version of generic mapping tools released. EOS Transaction of AGU, **79**(47), 579.

Wu, L., Xiao, A., Ma, D., Li, H., Xu, B., Shen, Y., & Mao, L. (2014). Cenozoic fault systems in southwest Qaidam Basin, northeastern Tibetan Plateau: Geometry, temporal development, and significance for hydrocarbon accumulation, *AAPG Bull.* **98**(6), 1213-1234.

Yokota, Y., Koketsu, K., Fujii, Y., Satake, K., Sakai, S.I., Shinohara, M. & Kanazawa, T., (2011). Joint inversion of strong motion, teleseismic, geodetic, and tsunami datasets for the rupture process of the 2011 Tohoku earthquake, *Geophys. Res. Lett.* **38**(7), 1, doi:10.1029/2011GL050098.

Full mailing addresses:

Mohammad Heidarzadeh:

Department of Civil & Environmental Engineering, Brunel University London, Uxbridge UB8 3PH, UK.

Email: mohammad.heidarzadeh@brunel.ac.uk

Takeo Ishibe:

Association for the Development of Earthquake Prediction, Tokyo 101-0064, Japan

Tomoya Harada:

Horihune 1-12-11, Kita-ku, Tokyo 114-0004, Japan

Danny Hilman Natawidjaja:

RC Geotechnology, Indonesian Institute of Sciences (LIPI), Bandung 40135, Indonesia

Ignatius Ryan Pranantyo:

Department of Civil & Environmental Engineering, Brunel University London, Uxbridge UB8 3PH, UK

Bayu Triyogo Widyantoro:

The Indonesian Geospatial Information Agency, Cibinong, Indonesia

List of Tables:

Table 1. M>7.0 earthquakes in the Molucca Sea double subduction zone in the past ~100 years

Number	Date (yyyy/mm/dd)	Longitude (deg.)	Latitude (deg.)	Depth (km)	M	Seismic Network
1	1913/03/14	126.121	5.354	15	7.8	USGS[*]
2	1925/05/03	126.304	1.19	15	7.1	ISCGEM[†]
3	1925/06/03	126.01	1.292	15	7.0	ISCGEM
4	1932/05/14	125.805	0.493	15	7.7	ISCGEM
5	1936/04/01	126.368	4.241	35	7.8	USGS
6	1936/10/05	126.354	1.642	15	7.0	ISCGEM
7	1938/10/10	126.585	2.379	15	7.3	ISCGEM
8	1947/06/12	126.156	1.201	15	7.0	ISCGEM
9	1968/08/10	126.234	1.514	23	7.6	ISCGEM
10	1985/04/13	126.411	1.622	51	7.0	US[‡]
11	1986/08/14	126.519	1.795	33	7.5	US
12	1989/02/10	126.76	2.305	44	7.1	US
13	2000/05/04	123.573	1.105	26	7.6	USGS
14	2001/02/24	126.249	1.271	35	7.1	US
15	2007/01/21	126.282	1.065	22	7.5	US
16	2014/11/15	126.5217	1.8929	45	7.1	US
17	2019/11/14	126.4144	1.6294	33	7.2	US

[*]: United States Geological Survey; [†]: International Seismological Center (ISC)-GEM Global Instrumental Earthquake Catalogue; [‡]: USGS National Earthquake Information Center US Catalog.

List of Figures:

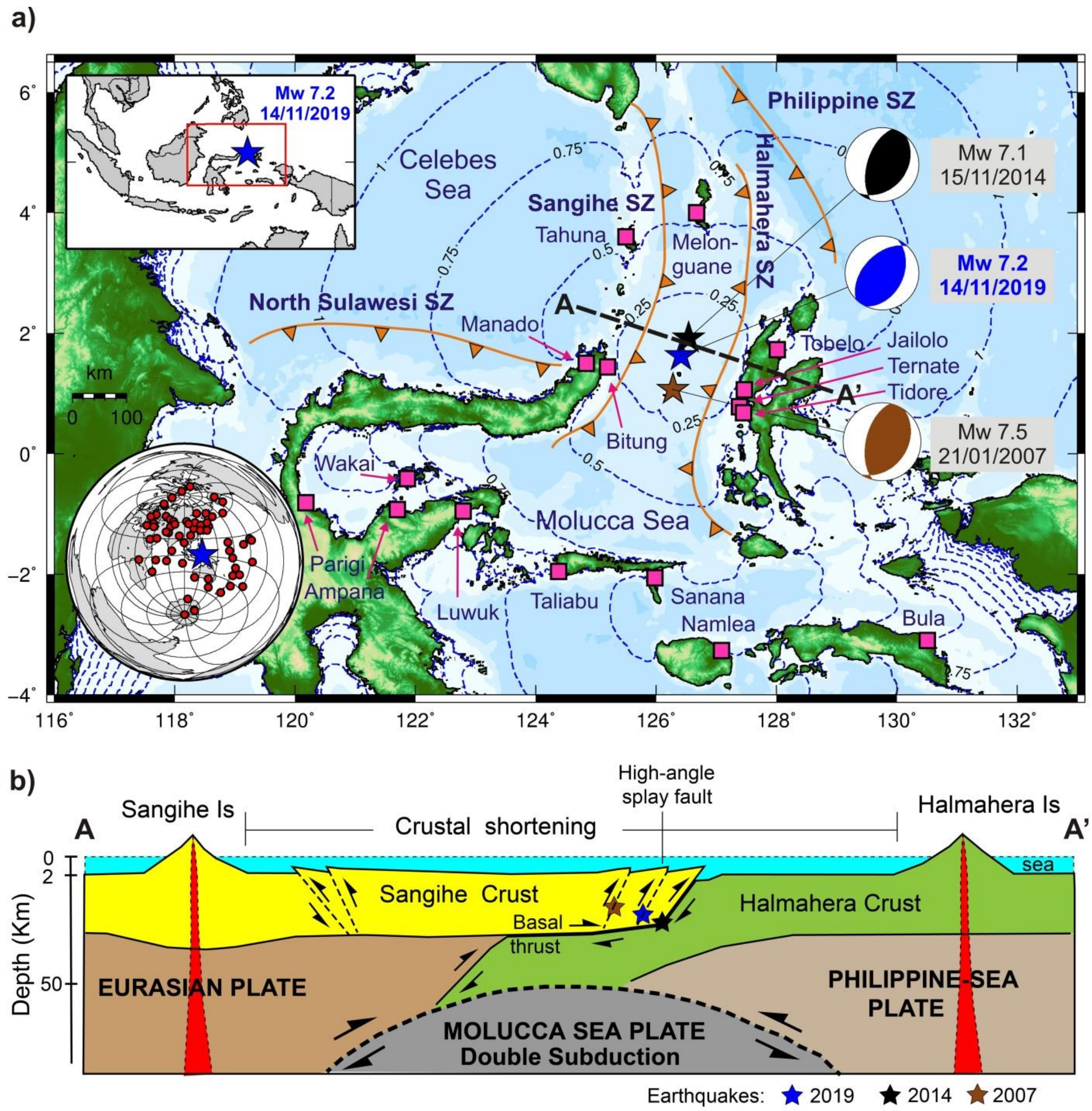

Figure 1. a) The location map of eastern Indonesia showing major subduction zones (brown thick lines), the epicenters (stars) and focal mechanisms of some recent events (based on the USGS catalogue) as well as locations of tide gauges (pink squares). The dashed contours indicate tsunami travel times in hours for the November 2019 earthquake. The inset at the bottom-left shows seismic stations used for teleseismic inversion. **b)** Sketch showing the arc-arc collision overlying the Molucca Sea divergent double subduction zone. The depths and locations of the earthquakes are approximated.

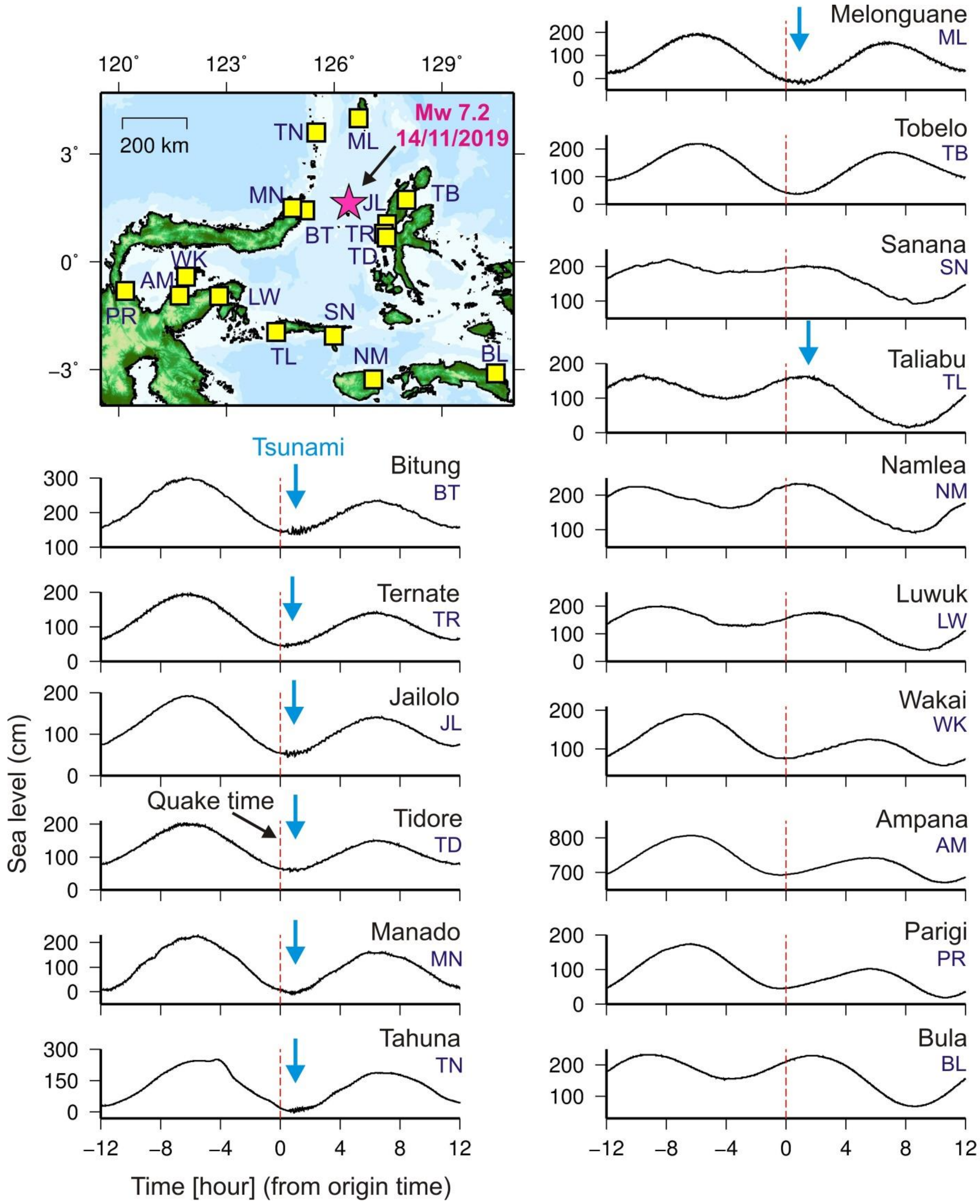

Figure 2. All tide gauge data used in this study for the analysis of the 14 November 2019 Molucca Sea M_w7.2 earthquake and tsunami. The blue arrows mark tsunami arrivals in each tide gauge stations. The abbreviated two-letter names in the map are spelled out in each waveform.

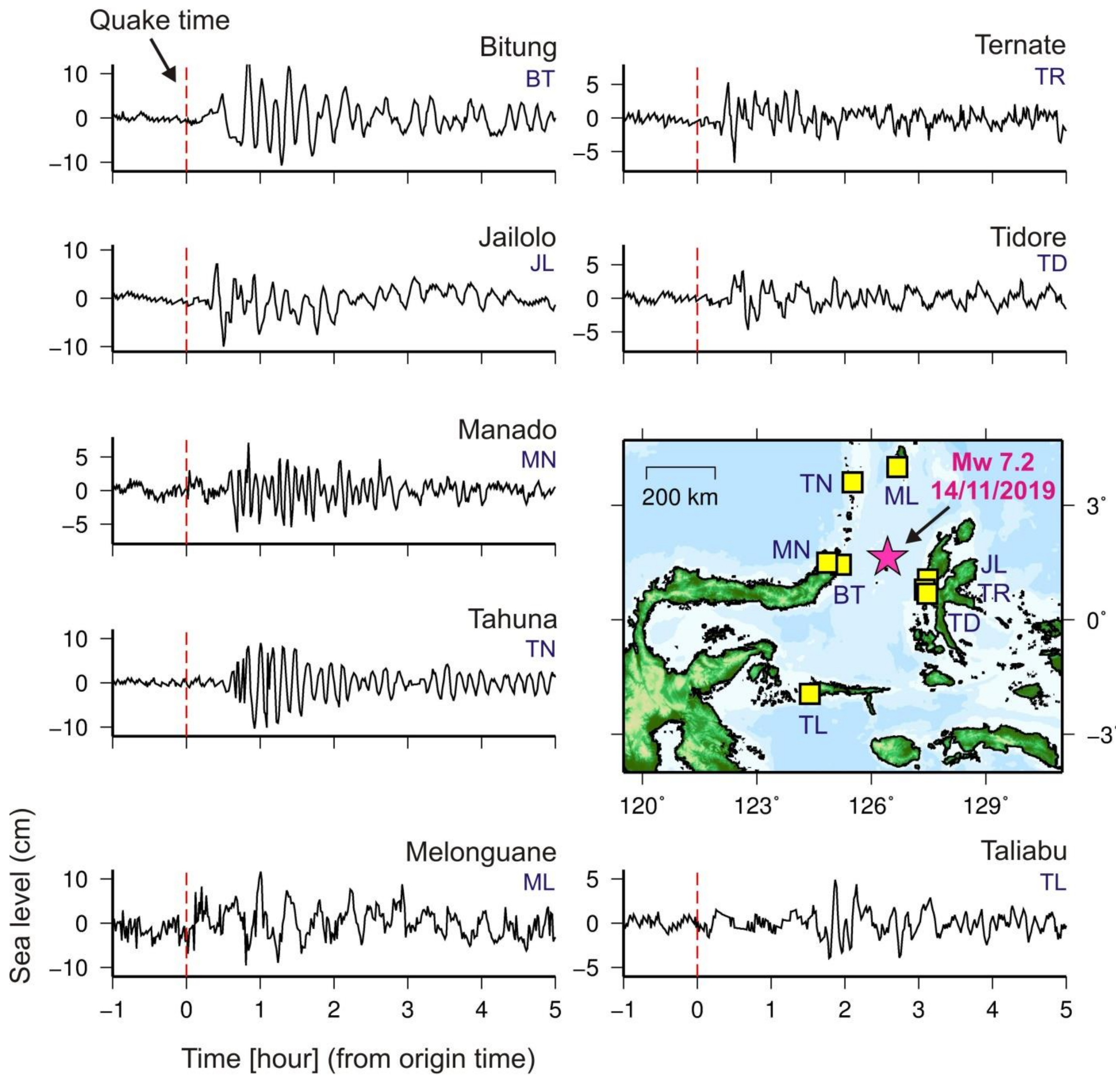

Figure 3. Tide gauge tsunami waveforms of the 14 November 2019 Molucca Sea M_w7.2 tsunami. These are the waveforms that are marked by blue arrows in Figure 2. The abbreviated two-letter names in the map are spelled out in each waveform.

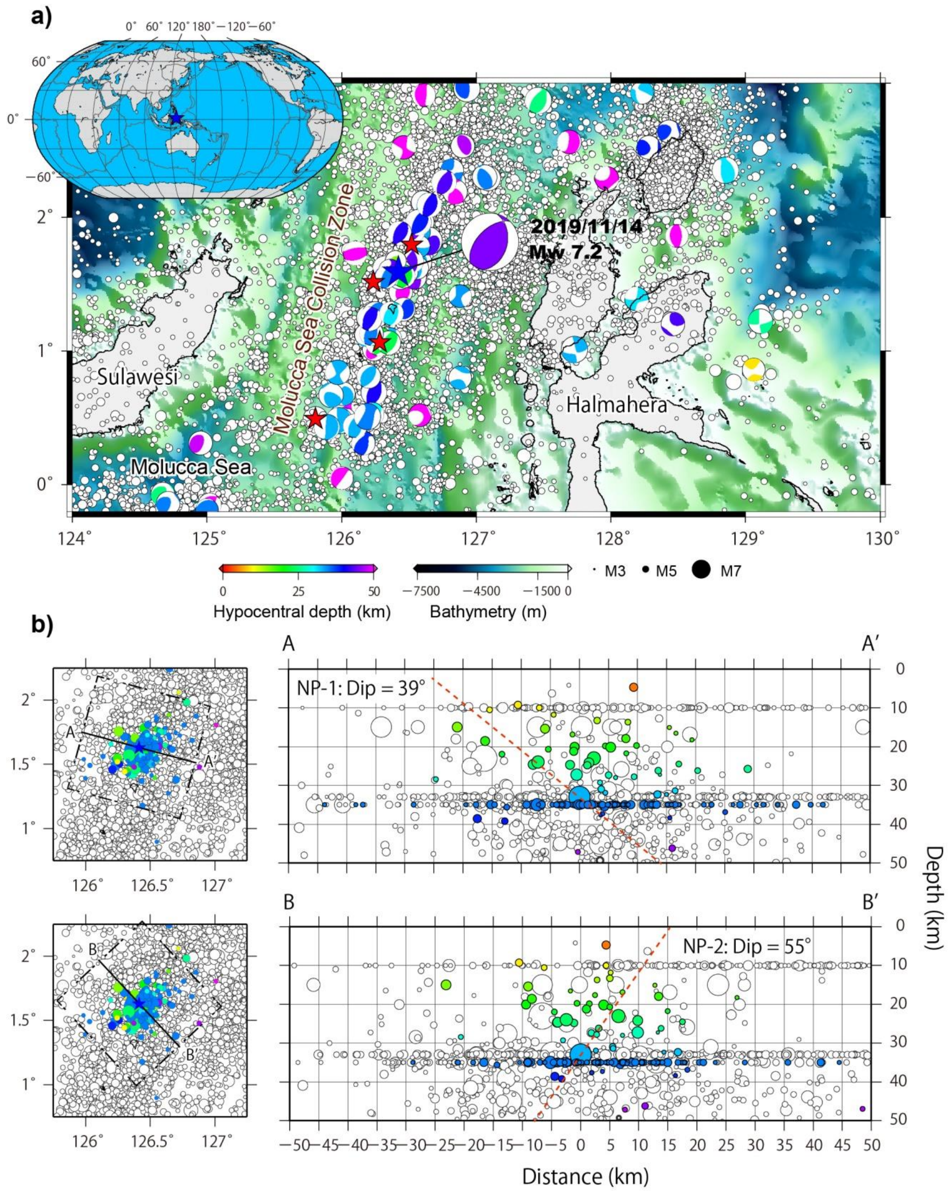

Figure 4. a) Seismicity of the Molucca Sea since 1910 (white circles) along with the focal mechanisms of major earthquakes. Data are from the USGS catalogue and the GCMT project. The blue star indicates the epicenter of the November 2019 event while the red stars show the epicenter of major (M7.5 or larger) earthquakes. **b)** Cross sections of the one-month aftershocks of 14 November 2019 Mw 7.2 earthquake (colored circles) and past seismicity (open circles) based on the USGS catalog perpendicular to the NP-1 (A-A’) and NP-2 (B-B’).

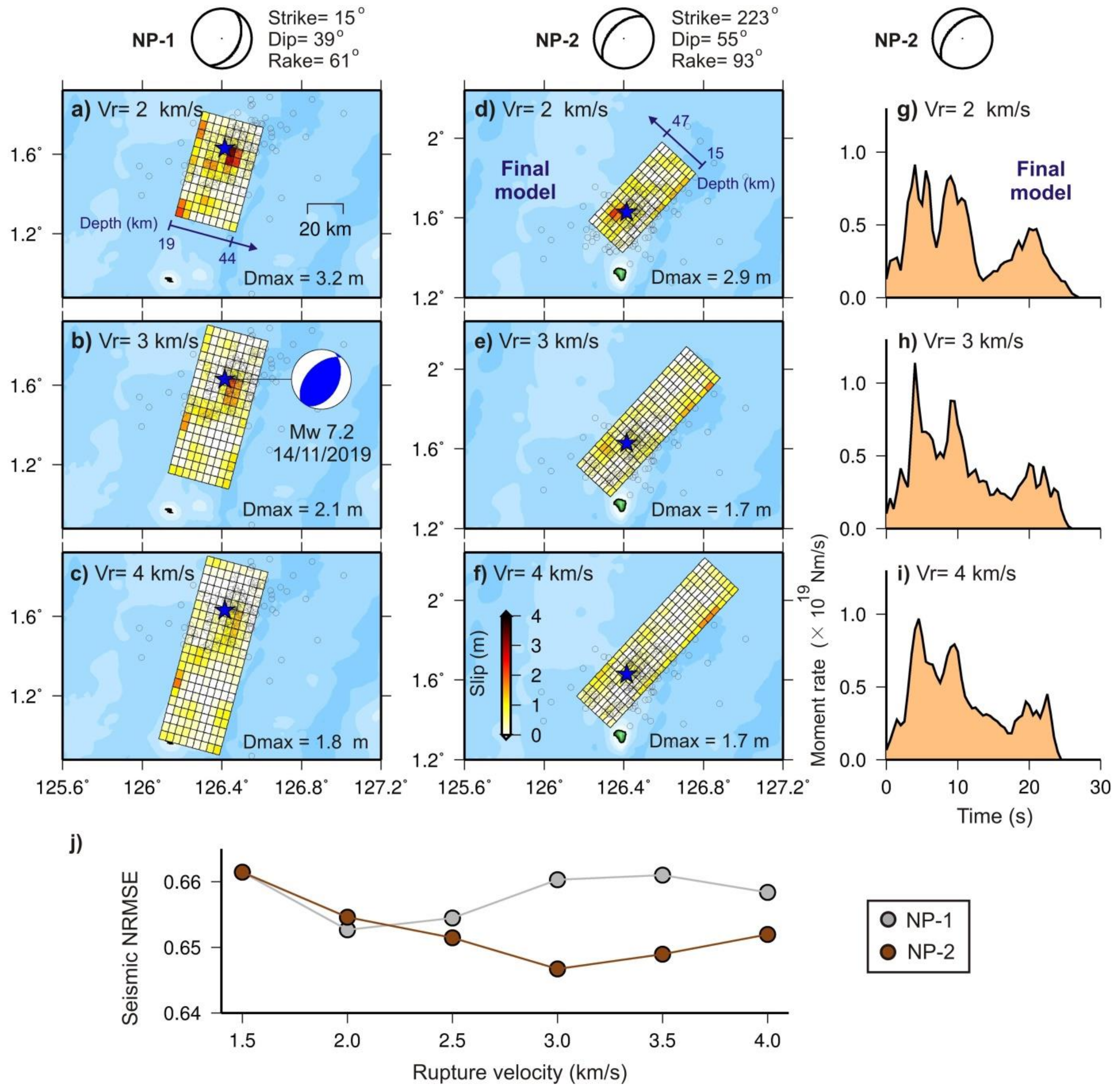

Figure 5. Results of teleseismic inversion. **a-c)** Slip distributions for the nodal plane 1 (NP-1) using different rupture velocities (V_r). **d-f)** Slip distributions for the nodal plane 2 (NP-2) using different V_r. Open circles show one-month aftershocks, while "Dmax" is the maximum slip amount. **g-i)** Source-time functions for NP-2 at different V_r. **j)** Normalized Root Mean Square Errors (NRMSE) of teleseismic inversion for both NPs at different V_r.

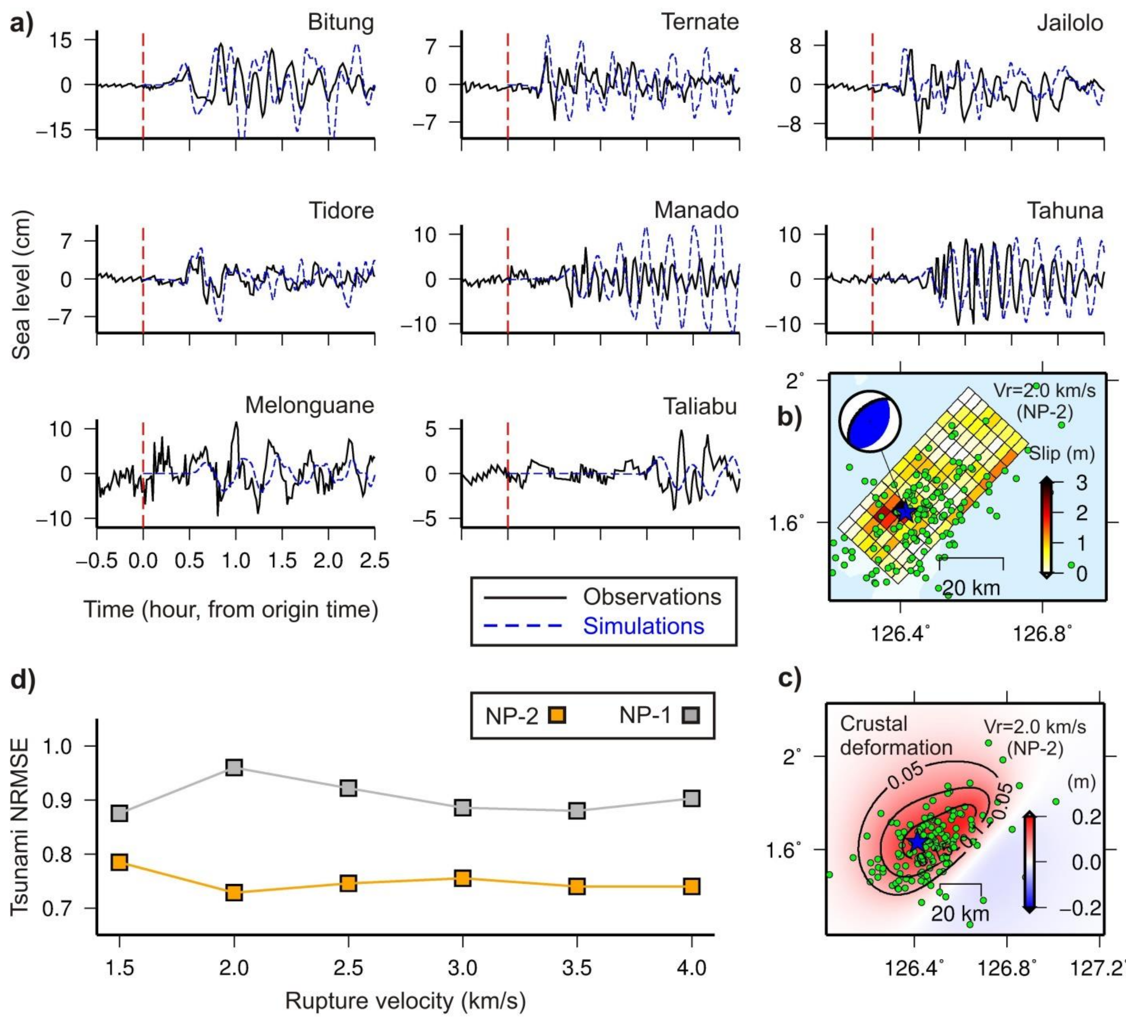

Figure 6. Results of tsunami simulations. **a)** Comparison of observed (black) and simulated (blue) tsunami waveforms for the final source model (NP-2; V_r =2.0 km/s). **b)** Slip distribution of the final source model. **c)** Crustal deformation due to the final source model. Green circles show one-month aftershocks. **d)** Normalized Root Mean Square Errors (NRMSE) of tsunami simulations for both NPs at different V_r.

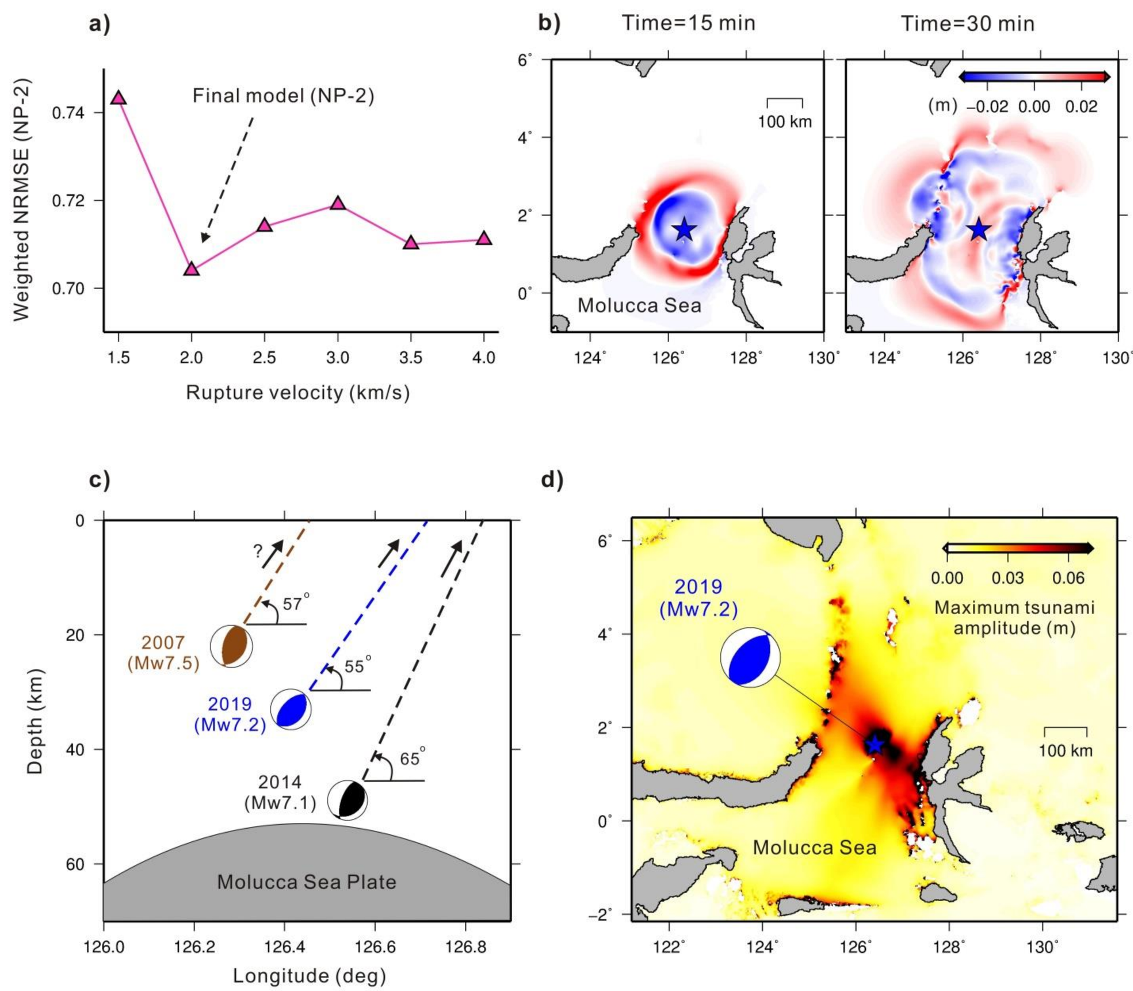

Figure 7. a) The weighted NRMSE of NP-2 considering 33.3% contribution from NRMSE of teleseismic inversion and 66.7% from NRMSE of tsunami simulation. **b)** Tsunami simulation snapshots at times 15 min (left) and 30 min (right) after the origin time. **c)** Sketch showing the dip angles of the three events of 2007, 2014 and 2019 in the Molucca Sea region. The question mark on the 2007 event indicates the fault plane has not been confirmed. **d)** Maximum tsunami amplitudes generated by the final source model (NP-2; V_r =2.0 km/s).